OPEN

Correspondence and
requests for materials
should be addressed to
J.H. (jianhe@clemson.
edu) or A.M.R. (arao@
g.clemson.edu)

Preferential Scattering by Interfacial Charged Defects for Enhanced Thermoelectric Performance in Few-layered n-type Bi_2Te_3

Pooja Puneet[1], Ramakrishna Podila[1,2,3], Mehmet Karakaya[1,3], Song Zhu[1], Jian He[1,3], Terry M. Tritt[1], Mildred S. Dresselhaus[4] & Apparao M. Rao[1,2,3]

[1]Department of Physics and Astronomy, Clemson University, Clemson, South Carolina, SC 29634 USA, [2]Center for Optical Materials Science and Engineering Technologies, Clemson University, Clemson, SC 29634 USA, [3]Clemson Nanomaterials Center, Clemson University, Clemson, SC USA 29634, [4]Department of Physics and Electrical Engineering, Massachusetts Institute of Technology, Cambridge, Massachusetts 02139, USA.

Over the past two decades several nano-structuring methods have helped improve the figure of merit (ZT) in the state-of-the art bulk thermoelectric materials. While these methods could enhance the thermoelectric performance of p-type Bi_2Te_3, it was frustrating to researchers that they proved *ineffective* for n-type Bi_2Te_3 due to the inevitable deterioration of its thermoelectric properties in the basal plane. Here, we describe a novel chemical-exfoliation spark-plasma-sintering (CE-SPS) nano-structuring process, which transforms the microstructure of n-type Bi_2Te_3 in an extraordinary manner without compromising its basal plane properties. The CE-SPS processing leads to preferential scattering of electrons at charged grain boundaries, and thereby increases the electrical conductivity despite the presence of numerous grain boundaries, and mitigates the bipolar effect via band occupancy optimization leading to an upshift (by ~ 100 K) and stabilization of the ZT peak over a broad temperature range of ~ 150 K.

Despite its simplistic nature and unique technical merits, thermoelectricity has previously found only a few *niche* applications mainly due to its low conversion efficiency[1,2]. For broader applications, it is crucial to develop high performance thermoelectric (TE) materials whose figure of merit (ZT) is in the neighbourhood of 2, where $ZT = \alpha^2 T / \rho \kappa_T = PF / \kappa_T$, and α is the thermopower (*i.e.*, Seebeck coefficient), ρ the electrical resistivity, κ_T the total thermal conductivity, T the absolute temperature, and PF the power factor. The inherent inter-dependence among α, ρ, and κ poses a major roadblock in realizing TE materials with higher ZT values[2,3]. In this context, tailoring the micro- and nano-structures at multiple length scales using advanced materials preparation methods has to a certain extent been able to decouple the inter-dependence among the TE properties; α, ρ, and κ[4,5].

However, with many TE elements (or materials) in a TE device, there are several secondary "limiting factors" besides ZT that must be overcome to achieve high TE device efficiency, *viz.*: (*i*) *suitability of n- and p-type materials*: a similar composition, performance, thermal and mechanical stability for the *n*- and *p*-legs of a TE device is required; (*ii*) *a wide operating temperature range for ZT*: in practice, a less temperature-dependent and a reasonably high *ZT* over a broad temperature range is desirable in contrast to a high *ZT* over a narrow temperature range; (*iii*) *a low electrode contact resistance*: for a given *PF*, a lower ρ is preferred over a higher α since the former results in a lower electrode contact resistance and thus lesser parasitic losses; and (*iv*) *a weak temperature dependence of the compatibility factor (Σ)*: a weakly temperature-dependent compatibility factor (ratio of the electrical current density to heat flux) is highly desirable[6–8]. Failure to properly address these limiting factors makes the effort of enhancing *ZT* futile. It is then quite pertinent to explore *nano-structuring processes* that improve *ZT* without adversely effecting factors (*i*)–(*iv*).

Since its discovery in 1950s[9], Bi_2Te_3 alloys have been probably the most widely studied and device utilized TE materials to date. More recently, Bi_2Te_3 has gained renewed interest as an intriguing example of a three-dimensional topological insulator[10,11]. In regards to its TE properties, state-of-the-art Bi_2Te_3 materials (typically, p-type $Bi_{0.5}Sb_{1.5}Te_3$ and n-type $Bi_2Te_{2.7}Se_{0.3}$) are the only TE materials that can be used for both power generation and

refrigeration with a room temperature value of $ZT \sim 1$[12]. A greater opportunity for an improved performance in these TE materials can be expected if the above limiting factors (*i*) to (*iv*) are mitigated. Thus far, researchers have successfully enhanced ZT in *p*-type Bi_2Te_3 by subjecting the bulk materials to nano-structuring processes, such as ball milling[13], melt spinning[14,15], thermal forging[16,17] and hydro-thermal synthesis[18,19], *etc.*, and melt-spun *p*-type Bi_2Te_3 ranks high in the list of current state-of-the-art TE materials with a room temperature $ZT \sim 1.5$[20]. In contrast, similar approaches have been ineffective so far in enhancing ZT in *n*-type Bi_2Te_3 due to its strong texture and highly anisotropic transport properties[21–24]. Compared to bulk *p*-type Bi_2Te_3, bulk *n*-type Bi_2Te_3 is easily cleavable[25] and traditional nano-structuring processes (*e.g.*, ball milling[26]) severely deteriorates its *in-plane* (basal plane) transport that is crucial for realizing potential high ZT *values*. Furthermore, the mismatch of grain boundaries adversely affects the electrical conduction, and hence an effective *nano-structuring process* is needed for *n-type* Bi_2Te_3 that *preserves the in-plane micro-morphology* to a maximum extent.

The chemical exfoliation method has been successful in generating quasi-two-dimensional materials, which exhibit the same basal plane properties as that of the parent bulk materials[27,28]. Upon densification of chemically exfoliated *n*-type Bi_2Te_3, one can then control structuring at micro- and nano- length scales, while preserving the basal-plane properties. Ideally, grain boundaries should exhibit multi-tier scattering, *i.e.*, they should scatter: i) phonons more effectively than charge carriers, ii) low energy charge carriers more effectively than high energy charge carriers (*i.e.*, energy filtering), and iii) holes (minority carriers) more effectively than electrons (majority carriers) in the case of *n*-type materials to suppress the bipolar effect[29,30]. In this article, we prepared bulk materials comprised of nanostructured *n*-type Bi_2Te_3 ($Bi_2Te_{2.7}Se_{0.3}$), and optimized its ZT over a broad range of temperature. We adopted a chemical exfoliation method, which resulted in few-layered *n*-type Bi_2Te_3 ($Bi_2Te_{2.7}Se_{0.3}$), and through transport measurements observed the multi-tier preferential scattering described above. Most importantly, we found that a combination of chemical exfoliation and spark plasma sintering (CE-SPS) enables one to attain the multi-tier preferential scattering in *n*-type Bi_2Te_3.

Results

A commercial state-of-the-art *n*-type Bi_2Te_3 ($Bi_2Te_{2.7}Se_{0.3}$) ingot exhibits a lamellar morphology with layers extending to hundreds of microns (Fig. 1a). Upon chemical exfoliation for 8 hours in N-methyl-2-pyrrolidinone (sample labelled as exf8h), the layer dimensions are reduced to 500–800 nm in length and a few tens of nm in thickness (Figs. 1b–c). Next, the exf8h samples were spark plasma sintered (see Methods section) to yield pellets (exf8h-SPS) whose TE properties and Raman spectra are discussed below. Interestingly, exf8h-SPS exhibited a lamellar micro-structure with an average thickness of 20–50 μm (Fig. 1d) which resulted from the stacking of exfoliated nano-sheets along the *c*-axis during the SPS process. Thus, the combined CE-SPS process introduced more grain boundaries/interfaces as evidenced in Fig. 1d, and the high-resolution powder x-ray diffraction (XRD) data (see *supplementary information*, Fig. S1) of exf8h-SPS corresponded to that of single phase $Bi_2Te_{2.7}Se_{0.3}$ (JCPDS card no. 00-050-0954). The broadening of the (0,0,6) peak (Table S1), as inferred from its full-width at half maximum intensity or FWHM ($\delta\theta$) for the exf8h sample is consistent with the formation of few-layered nano-sheets (*cf.* Figs. 1b–c). Furthermore, the average values for the coherence length (δL) showed a significant increase for the exf8h-SPS sample along the (0,0,6) direction while the coherence length did not change significantly along the (1,1,0) direction (see *supplementary information*, Fig. S1 and Table S1). Such observations imply that the *crystallinity or the long-range order is improved* due to spark plasma sintering of
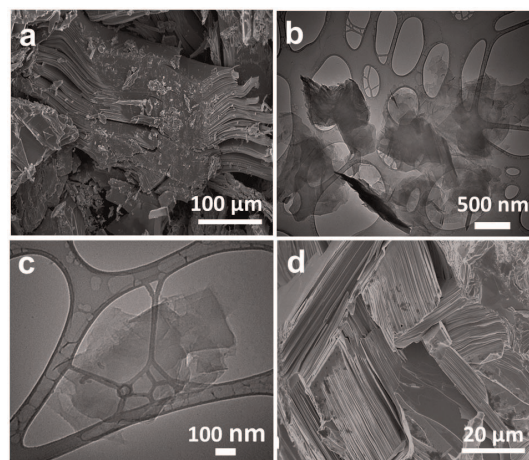

Figure 1 | (a) A representative scanning electron micrograph of commercially available state-of-the-art *n*-type Bi_2Te_3 ingot. Panels (b) and (c) show representative transmission electron micrographs for a chemically exfoliated sample (exf8h), and (d) shows a representative image for the exfoliated sample subjected to the SPS process (exf8h-SPS).

exf-8h samples despite the use of high-energy processes such as ultrasonication and SPS.

Discussion

The temperature dependences of α, ρ, and κ of exf8h-SPS samples are compared in Fig. 2 with the corresponding properties of state-of-the-art *n*-type Bi_2Te_3 ingot. It is noteworthy that all transport properties were measured in the same direction (perpendicular to the SPS direction; see supplementary information, Fig. S3) and reproduced on *at least* 3 samples. Furthermore, the low and high temperature measurements performed using two different techniques showed an excellent match for all transport properties. As shown in Fig. 2a, the peak thermopower value (α_{max}) for exf8h-SPS samples decreased and shifted towards higher temperatures, in agreement with the Goldsmid-Sharp relation[31]. The upshift in α_{max} to higher temperature suggests that the bipolar contribution (of holes) to the electrical conduction occurs at a relatively higher temperature in exf8h-SPS, compared to that for the ingot. Although the α values for the exf8h-SPS are relatively lower in magnitude, its metal-like electrical resistivity (Fig. 2d) was found to be lower for $T > 100$ K making the power factor values (Fig. 2b) comparable to that of the ingot. Indeed, the net reduction of α for the exf8h-SPS samples is related to a decrease in the ρ as expected from the inverse coupled behaviour. It is interesting to note that the ρ of exf8h-SPS samples decreases relative to the commercial ingot despite the increase in the density of grain boundaries. Such a result is unexpected since an increase in grain boundaries is expected to result in increased scattering of charge carriers, and consequently a higher ρ. In order to gain a deeper understanding of the origin of this unexpected decrease in ρ, we performed Hall measurements to estimate the carrier concentration (n) and mobility (μ). Inferring from Figs. 3a–b, the observed decrease in ρ is clearly associated with an increase in the n at $T >$ 100 K. Previously, Teweldebrhan *et al.*[25] reported that the chemical/mechanical exfoliation of bulk Bi_2Te_3 leads to two kinds of products, those cleaved at the van der Waals gap (see Fig. S2) in which the quintuple units remain intact, and those in which the cleavage occurs within the quintuple units leading to donor-like defects with positively charged Te_{Bi} anti-sites/Te vacancies on the surface/boundaries of the exfoliated grains[32] (see Fig. 3c). As shown in the schematic in Fig. 3c–e, such localized positive charges on the grain boundaries are known to inject excess electrons into the bulk material, thereby increasing n[13]. More importantly, any positively charged defects on the grain boundaries (hence forth referred as *interfacial charged*
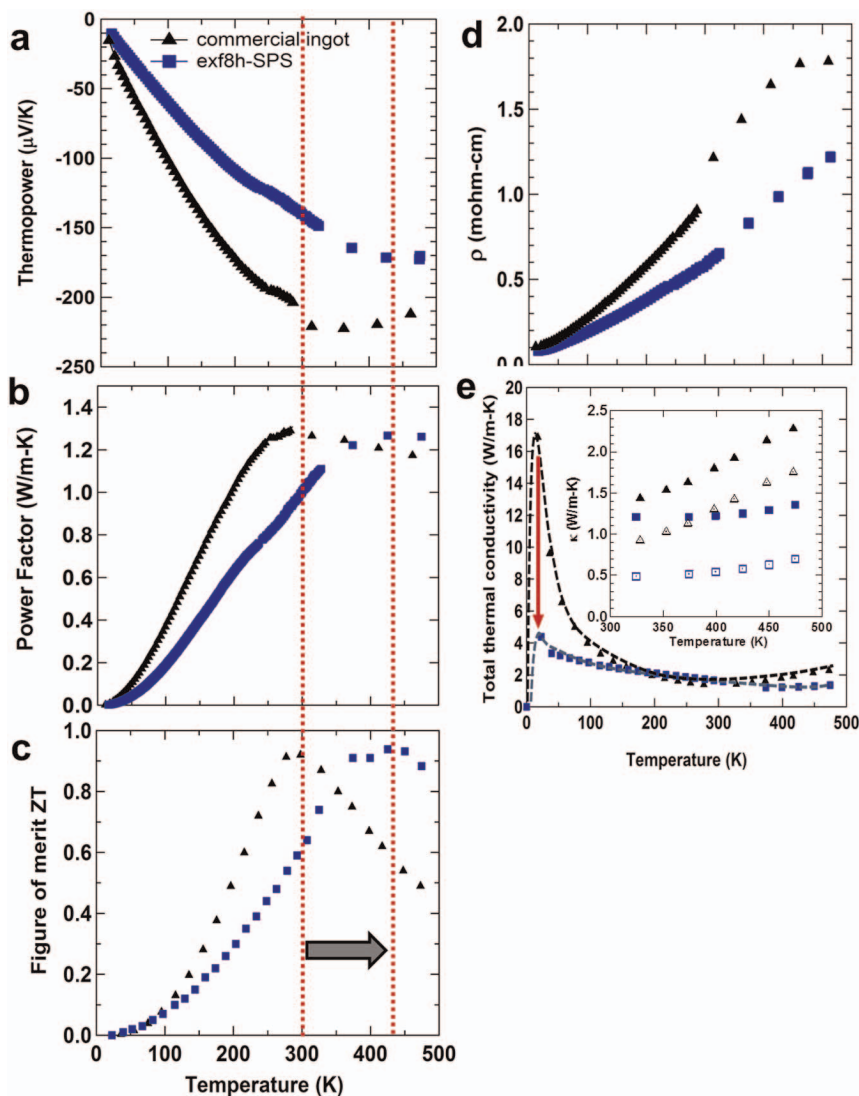
Figure 2 | Temperature dependence of the thermopower α (a), power factor $\alpha^2 T/\rho$ (b), dimensionless figure of merit ZT (c), resistivity ρ (d), total thermal conductivity κ_{Total} (e) of the exf8h-SPS sample and the commercial n-type Bi_2Te_3 ingot. The arrow in panel c highlights the shift in the ZT peak position for the exf8h-SPS sample. In Panel (e), the down-pointing red arrow shows the decrease in magnitude of κ_T due to smaller grain size of the exf8h-SPS sample. The inset figure in (e) represents an expanded view of κ_T vs. T for T > 300 K, and also shows the temperature dependence of $(\kappa_T - \kappa_e)$ for the ingot (open triangle) and the exf8h-SPS sample (open squares).

defects) act as a potential barrier (Fig. 3e), which selectively filters low-energy minority carriers (holes in the case of n-type Bi_2Te_3) and thereby shifts the onset of bipolar effects (two carrier conduction) to a higher temperature (*cf.* Figs. 2a, b and e). This bipolar shift also applies to the $(\kappa_T - \kappa_e)$ of the sample and is discussed below.

Interestingly, the μ of the exf8h-SPS sample shows lower values for $T < 100$ K despite its improved crystallinity relative to the commercial ingot (Fig. 3b). This decrease in μ is due to additional scattering arising from the charged defects present at the interfaces (Fig. 3d). Depicted in Fig. 3b are various temperature dependent scattering processes that are known to limit μ of electrons according to Matthiessen's rule[33]. Evidently, the temperature dependence of μ for the exf8h-SPS sample deviates from that of the commercial ingot for $T < 100$ K, possibly due to an increased contribution to carrier scattering arising from charged defects ($\sim T^{3/2}$) and grain boundary scattering ($1/_T exp\left(\dfrac{-e\phi_a}{k_B T}\right)$); where ϕ_a is the barrier potential due to the interfacial charged defects and κ_B is the Boltzmann constant). For $T < 100$ K, the electrical resistivity ($\rho = 1/\sigma$, where $\sigma \propto ne\mu$) of the exf-8h and ingot samples was approximately the same since the increase in n is compensated by a decrease in μ. For $T > 100$ K,

the mobility of both the samples exhibited the same values, implying that the decrease in ρ is entirely due to the increase in n. As a result of the upshift in α_{max}, the bipolar term in the thermal conductivity is also shifted to higher temperatures (*cf.* Fig. 4a) and hence the total κ above 300 K shows smaller values for the exf8h-SPS samples relative to the commercial ingot (*cf.* Fig. 2e). The evident reduction in the magnitude of the $\kappa_{lattice}$ peak (shown by the red down-pointing arrow in Fig. 2e) confirms that new long-range phonon scattering centres (*e.g.*, grain-boundaries/interface) are introduced by exfoliation and the subsequent SPS process, *i.e.*, the CE-SPS process. It is important to measure all thermoelectric properties in the same direction to avoid an overestimation of ZT. For this reason, we consistently measured κ in the same direction as α and ρ (*cf.* Fig. S3) according to a protocol we developed previously[34]. Consequently, the upshift due to the bipolar contribution leads to the observed upshift of ZT peak to higher temperatures (Fig. 2c). A detailed discussion and the underlying mechanism for this upshift are presented in the following sections. Furthermore, the concomitant changes in α, ρ, and κ are nearly balanced out in the exf8h-SPS sample for $T > 300$ K, making ZT values constant ($\sim$1.0) in the range of 380–500 K.
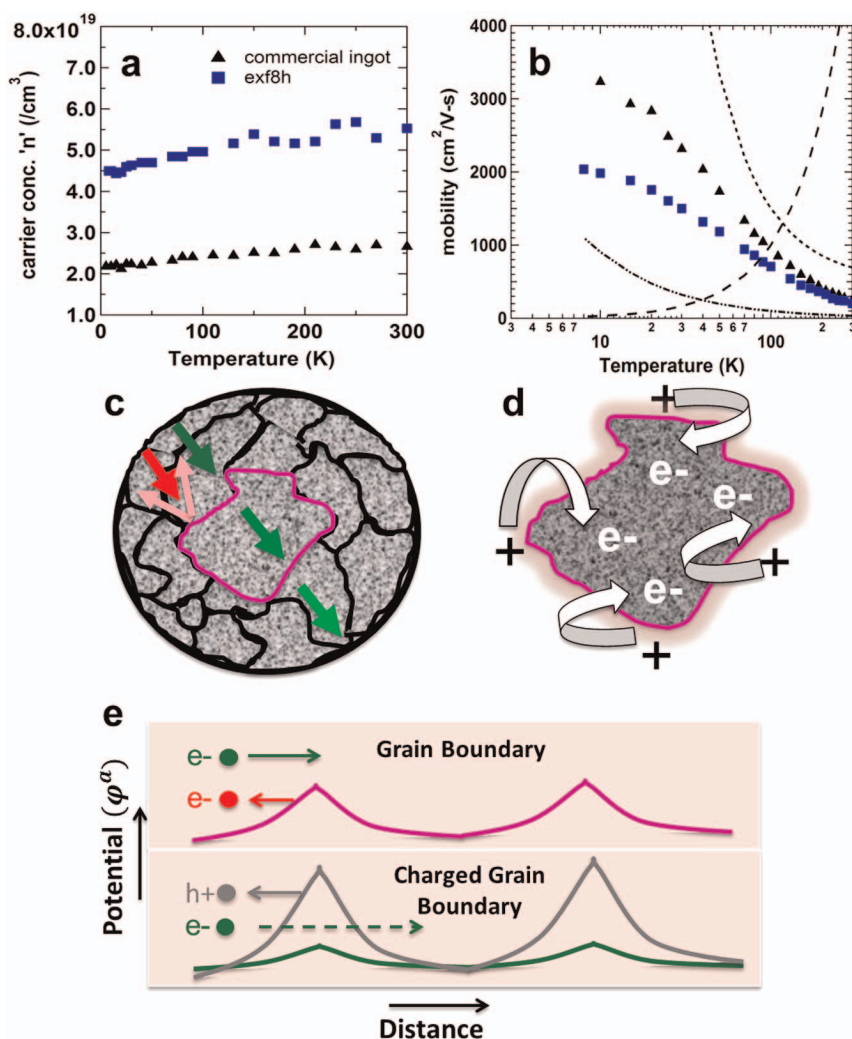
Figure 3 | Temperature dependence of carrier concentration n (panel a) and electron mobility μ (panel b) for a commercial ingot and the exf8h-SPS sample. For $T < 100$ K, the grain boundary and charged defect scattering dominates, and for $T > 100$ K, the electron-phonon scattering dominates. The dotted lines in panel b represent the temperature dependence of various scattering mechanisms, *viz.* grain boundary ($\frac{1}{T}exp\left(\frac{-e\phi_a}{k_BT}\right)$), charged defect ($\sim T^{9/2}$) and electron-phonon ($\sim T^{-3/2}$) scattering processes. A schematic depicting of the grain boundaries scattering of charge carriers in *n*-type Bi_2Te_3 system (panel c) shows that low kinetic energy carriers (represented by red arrow) are effectively scattered by the grain boundary potential barrier (ϕ_a) unlike high kinetic energy carriers (represented by green arrows). (d) The presence of a positively charged donor-like grain boundary defect (arising from Te vacancies and Te-Bi anti-sites) can inject excess charge carriers into the core of the grain resulting in an increase of carrier concentration (*cf*. Fig. 5a). (e) The positively charged grain boundary leads to selective scattering of holes over electrons due to increased Coulomb barriers. Such a preferential scattering mechanism is responsible for the observed temperature upshift in the bipolar contribution to transport properties of exfoliated *n*-type Bi_2Te_3.

The Debye temperature (θ_D) of pristine Bi_2Te_3 is known to be ~ 145 K[35]. At sufficiently high enough temperatures (close to θ_D), the phonon-phonon scattering dominates due to the *Umklapp processes* and therefore the lattice thermal conductivity exhibits a ($1/T$)-temperature dependence as shown in Eq.1[36]

$$\kappa_L = 3.5 \left(\frac{k_B}{h}\right)^2 \frac{MV^{1/3}\theta_D^3}{\gamma^2} \frac{1}{T}, \quad (1)$$

where M is the average mass per atom, V is the average atomic volume, γ is the Grüneisen parameter and h is Planck's constant. At higher temperatures ($T > 300$ K), the linear increase in the thermal conductivity with temperature can be explained by the dominating bipolar conduction in the system. The bipolar diffusion contribution to κ_T arises when both holes and electrons contribute to conduction. The bipolar thermal conductivity (κ_B) can be expressed as $\kappa_B = \frac{\sigma_e\sigma_h(\alpha_e - \alpha_h)^2}{\sigma_e + \sigma_h}T$, where α_e (σ_e) and α_h (σ_h) are

specific contributions of electron and hole carriers to the thermopower (electrical conductivity) respectively[37]. As shown in Fig. 4a, ($\kappa_T - \kappa_e$) is plotted against $1000/T$ for the temperature range where the U-process dominates ($T > 100$ K). Since, $\kappa_T = \kappa_L + \kappa_e + \kappa_B$, the temperature dependence of $\kappa_T - \kappa_e$ can serve as a gauge for the interplay between the lattice and bipolar effects. Clearly, the commercial ingot samples exhibited the expected linear behaviour with respect to T^{-1} (from phonon-phonon scattering related to κ_L in Eq. 1) above the red dashed line at ~ 2.5 K^{-1} in Fig. 4a, while bipolar effects dominated at higher temperatures ($1000/T \sim 2.75$ or $T > 400$ K). Intriguingly, the exf8h-SPS samples showed an evident deviation from the linear behaviour in κ_L in the intermediate range (100 K $< T <$ 200 K) indicating the presence of an additional scattering process, which is consistent with interfacial charged defect scattering. Furthermore, the net reduction in κ_L, highlighted by the grey area in Fig. 4a, can be attributed to the increased number of grain boundaries in the exf8h-SPS sample. Most importantly, the ~ 100 K
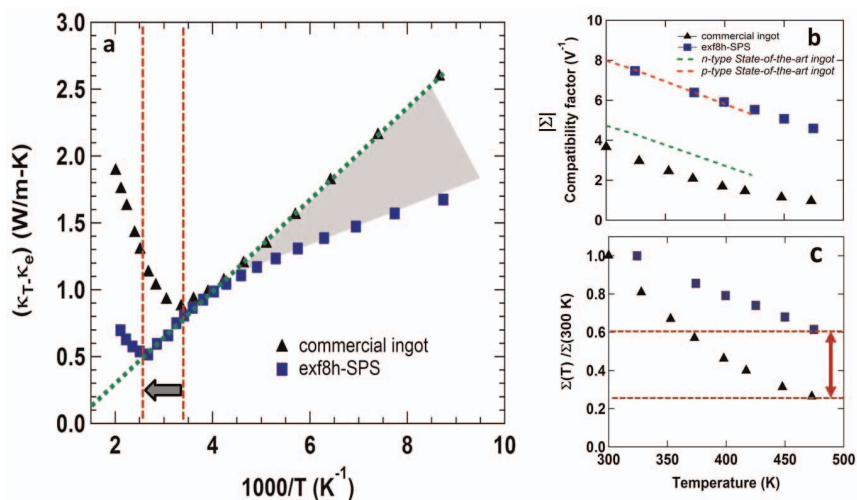
4

Figure 4 | (a) The ($\kappa_T - \kappa_e$) *vs* 1000/T plot is shown for the commercial ingot and the exf8h-SPS sample. For T < 300 K, phonon-phonon scattering dominates due to the U-process and κ_L varies as *1/T* (shown by the dotted line). The exf8h-SPS sample shows a shift of the bipolar term to higher temperature relative to the commercial ingot, as shown by the vertical dashed lines. This shift in temperature corresponds to the shift in the ZT peak. The deviation from 1/T behavior in the exf8h-SPS sample is shown in grey, which may arise due to an additional scattering mechanism dominating in the intermediate temperature range. (b) Compatibility factor $|\Sigma|$ as a function of temperature is shown for our exfoliated sample in comparison with state-of-the-art *n*- and *p*-type ingots and (c) $\Sigma(T)/\Sigma(300$ K) is plotted as a function of temperature. The red arrow shows a smaller fractional change of compatibility factor in the exf8h-SPS samples when operating in the temperature range of 300–500 K relative to the state-of-the-art commercial n-Bi$_2$Te$_3$ ingot.

upshift (indicated by the left pointing arrow in Fig. 4a) in the exf8h-SPS sample due to bipolar contributions does not occur until 400 K (1000/$T \sim$ 2.5 in Fig. 4a), which is again consistent with the shift observed in the electrical transport measurements. Finally, it is possible to delineate the individual contributions of the electronic (κ_e), lattice (κ_L) and bipolar conduction processes to κ_T based on their temperature dependences in different temperature regimes. This is based on the assumption that the dominant mechanisms contributing to the phonon conduction in this system are the electronic, lattice and bipolar conduction processes for κ_T. A summary of estimated values and their percentage contributions to κ_T for the commercial ingot and exfoliated sample are shown at two different temperatures (Table S2) along with the individual contributions in Figure S3 (graph of the ($\kappa_T - \kappa_e$) *vs.* 1000/T). For details, please see supplementary information section, Figure S3–S4.

Thus far, we have explained the effects of the exfoliation on the TE properties of *n*-type Bi$_2$Te$_3$. An obvious question that arises is the following: Is it necessary to exfoliate *n*-type Bi$_2$Te$_3$ to a single-layer level in order to achieve improved TE performance? To address this question, we performed a detailed study in which we monitored the effects of exfoliation time on α, ρ, and κ. Interestingly, we observed that the α and ρ are nearly independent of the exfoliation times greater than 3 hours (from 3 to 8 hours), thereby leading to similar power factor values in the higher temperature range for all the samples (see Fig. S6). This observation of similar power factor values indicates that TE performance saturates beyond 3 hours of exfoliation time suggesting that a single-layer level is not necessary to achieve optimal properties. We have also performed detailed atomic force microscopy (AFM) and micro-Raman spectroscopic measurements in order to further elucidate the effects of exfoliation on layer thickness and the introduction of defects. Our AFM studies (Fig. S7) showed that the layer thicknesses vary from $\sim$ 1–5 μm in the bulk to $\sim$ 120 nm in exf3h samples, indicating that the quintuple cell in *n*-type Bi$_2$Te$_3$ is cleaved beyond the van der Waals gap during exfoliation. Upon exfoliation, the layer thickness of the exf5h samples reduced to $\sim$ 50 nm, and remained unchanged with extended exfoliation time. These results explain why the TE properties of the exf3h-SPS, exf5h-SPS, and exf8h-SPS samples are nearly the same (Fig. S6).

As shown in Fig. 5, the micro-Raman spectra of the exfoliated samples exhibited some interesting features that confirmed the presence of exfoliation-induced defect centers. The low frequency region (60–150 cm^{-1}) showed the presence of E_g^2, and A_{1g}^2 modes for all samples, and no discernible shift in the Raman peak positions was observed. Notably, we observed the emergence of new modes in the mid-frequency region (200–400 cm^{-1}) exfoliated *n*-type Bi$_2$Te$_3$. Interestingly, the sharp feature at $\sim$ 760 cm^{-1} was found to increase in intensity with increasing exfoliation time (inset figure in Fig. S6). These new features in the micro-Raman spectra are tentatively attributed to combination and overtone modes that arise due to defect-induced symmetry breaking[38,39]. A detailed Raman study will be published elsewhere.

In ideal TE devices, the TE properties must remain optimal over a broad operating temperature range. It is commonplace in practice that different materials are often segmented together, with each material operating in its most efficient temperature range, for an overall optimal efficiency of the TE device. Under such constraints, the optimal efficiency is obviously limited by the properties of the segmented materials[6,7]. The compatibility factor (Σ) of a TE material is defined in terms of α and ZT as[6]:

$$\Sigma = \frac{\sqrt{1+ZT}-1}{\alpha T},\qquad(2)$$

Σ for various materials used in the segmentation should be similar in order to achieve high device efficiency. If Σ of the segmented materials differs by a factor of two, the segmentation suffers parasitic losses, thereby lowering device efficiency[7]. As shown in Fig. 4b, the compatibility factor of exf8h-SPS is appreciably higher than that of the *n*-type commercial ingot and matches that of *n*-type PbTe ($\sim$3.5 V^{-1} at 500 K) in the maximum operating temperature range of both the materials[7], making it suitable for segmentation without inflicting substantial parasitic losses. Ideally, Σ should be a temperature independent parameter. However, the strong temperature dependence of α and ZT values often leads to a Σ that varies with temperature, making it difficult to optimize the heat and electric current densities along the TE leg that are necessary to take advantage of a large ZT. Therefore, one of the major concerns for developing Bi$_2$Te$_3$-based TE devices is the change in the Σ over the operating temperature range.
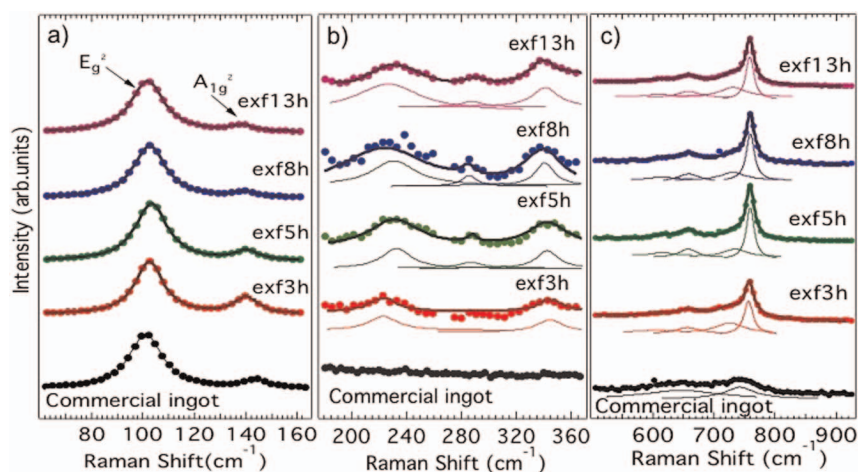
5

Figure 5 | Micro-Raman spectra of the commercial *n-type* Bi$_2$Te$_3$ ingot and the exfoliated samples in the low (panel a), mid (panel b), and high-frequency regions (panel c). Although there are no significant changes in the low-frequency region (panel a), the mid- and high-frequency regions (panels b and c) show the presence of distinct peaks that possibly arise due to defect-induced symmetry breaking. Importantly, the sharp peak at ~ 760 cm^{-1} (in panel c) is observed to change with exfoliation time as shown in the inset of Fig. S6.

To account for the variation of Σ as a function of temperature, some materials are often crafted into different shapes to maintain a constant current density throughout the *n-* or *p-type* legs. Such shaping effects can result in mechanical instability of the device if Σ varies greatly with temperature. In this regard, it is desirable to have a low fractional change in Σ for robust TE device integration. As shown in Fig. 4c, exf8h-SPS samples exhibit a significantly lower fractional change in Σ compared to a state-of-the-art commercial *n-type* Bi$_2$Te$_3$ ingot in 300–500 K range indicating that the CE-SPS processed samples are better suited for device integration. Furthermore, the CE-SPS processed samples showed constantly high *ZT* values from 380–500 K along with Σ values with smaller fractional change from 300–500 K, as well as better compatibility with probable higher temperature TE materials. These advances are critical for the integration of existing non-traditional materials into TE devices.

In summary, we show that a combined chemical exfoliation/SPS technique can mitigate the limiting factors discussed in the introductory paragraph, and can lead to the synthesis of *n-type* Bi$_2$Te$_3$ with desirable TE properties over a broad temperature range. Particularly, chemical exfoliation allows for the introduction of micro-and nanostructured scattering centres at multiple length scales while preserving the basal plane properties needed for preserving high *ZT* values. In our method, the possible introduction of interfacial charged defects (Te$_{Bi}$ antisites/Te vacancies) resulted in: *i*) the injection of electrons into the bulk, thereby increasing the carrier concentration, and *ii*) the introduction of a potential barrier that selectively filtered low-energy minority carriers (holes in the case of *n-type* Bi$_2$Te$_3$ samples), thereby shifting the onset of bipolar effects. Our micro-Raman spectra exhibited distinct features in the mid- and high-frequency ranges for exfoliated samples confirming the interfacial charge defect-induced symmetry breaking. Another evidence of an additional scattering mechanism in the exf8h-SPS sample is provided by our thermal conductivity data in the intermediate temperature range. An estimation of the bipolar contribution to the thermal conductivity clearly shows a shift in the temperature region where the bipolar effects dominate. The change in the onset of bipolar effects results in the shift of the *ZT* maxima and at the same time broadens the operating temperature regime. A slight reduction and a shift in the peak of α is balanced by decrease in ρ and κ, leading to peak *ZT* values, which are same as the commercial ingot. Lastly, the reduction of α while keeping the *ZT* values constant increases the compatibility factor.

Methods

Preparation of nanostructured bulk n-type Bi$_2$Te$_3$ samples. In this work, we achieve nano-structuring via a solvent exfoliation technique of optimized state-of-the-art *n-type* Bi$_2$Te$_3$ ingot samples (purchased from Marlow industries) with a chemical composition Bi$_2$Te$_{2.7}$Se$_{0.3}$. Exfoliated sheets were sintered together to form nanostructured bulk samples using a Spark plasma sintering (SPS) system.

The chemically exfoliated few layer nanosheets of a commercial ingot with a chemical composition Bi$_2$Te$_{2.7}$Se$_{0.3}$ were obtained by an ultra-sonication technique. For solvent exfoliation, bulk Bi$_2$Te$_{2.7}$Se$_{0.3}$ ($\sim$1 g) was dispersed in 100 ml of N-methyl-2-pyrrolidinone (NMP) and sonicated using 1/8" tip sonicator (Branson 250) at 100 W for 1 hr. The resulting dispersion was filtered through a 0.45 µm nylon filter and re-suspended in 100 ml of fresh NMP. Subsequently, the solution was bath sonicated for 3, 5, or 8 hrs and centrifuged at 2000 rpm for 45 min. The supernatant was vacuum filtered using a 0.45 µm nylon filter. Finally, the filtered powder was washed several times using deionized water to remove residual NMP. As a result of ultra-sonication, exfoliated few layer nano-sheets $\sim$ 10–15 nm in thickness and < 1 µm in length were obtained (*c.f.* Fig. 1d). Further, the exfoliated sheets were compacted using spark plasma sintering (SPS, Dr. Sinter Lab®-515S system) technique. In our previous studies on *p-type* Bi$_2$Te$_3$, we observed that a higher SPS temperature and a low SPS pressure results in better thermoelectric properties owing to better electrical connectivity and small textural effects[34]. Hence, we used similar conditions where the samples were sintered at 500°C and 30 MPa pressure under a dynamic vacuum in this study. Before the SPS process, the samples were loaded into graphite dies, and graphite rods were used to apply the pressure. The resulting SPS pellets were 12.5 mm in diameter and 2–3 mm in thickness. The SPS process yielded samples with 98–99% of the theoretical density.

Characterization. The microstructural and chemical analysis was performed using conventional SEM (Hitachi® S3400N and S4800), TEM (Hitachi® H7500) and high-resolution XRD characterization methods (Rigaku Ultima® IV diffractometer, Cu Kα radiation, $\lambda = 1.5406$ Å). Furthermore, micro-Raman spectra was taken on all the samples to observe any symmetry breaking or crystal structure changes using a Dilor XY triple grating monochromator with an excitation wavelength of 514.5 nm.

Transport property measurements. Low temperature (in the range of 20–325 K) resistivity ($\rho = 1/\sigma$) and α were measured using a four-probe differential method on a custom-designed system[40]. In addition, the thermal conductivity (κ_T) was measured *on the same sample* using a four probe steady-state method on a custom designed system from 20–320 K[41]. Both systems used custom designed measurement programs developed in our laboratory using Labview® software. The high temperature electrical resistivity and thermopower were simultaneously measured using the commercial ZEM-2 (Ulvac Riko, Inc.) system under low pressure of a high purity He atmosphere. The high temperature thermal conductivity was calculated using the relation $\kappa_T = \rho_D C_p D$; where ρ_D is the packing density of the material, D the thermal diffusivity and C_p ($\approx C_V$, for solids) the specific heat capacity. The heat capacity measurements were carried out using a NETZSCH® DSC 404 C, thermal diffusivity was measured using a NETZSCH® LFA 457 system and the packing density was measured by the Archimedes principle. The lattice contribution of the thermal conductivity was calculated by subtracting the electronic portion from κ_T. The electronic thermal conductivity was calculated using the Wiedemann-Franz relation ($\kappa_e = L_0 T/\rho$, where $L_0 = 1.66 \times 10$-8 V^2/K^2 for the nanostructured sample[42]).

It is important to note that the laser flash measures the diffusivity along the SPS pressure direction, whereas the low temperature transport properties are measured

along the direction perpendicular to SPS direction (*in the plane* of pellet). The anisotropy in the transport properties along different directions may lead to erroneous interpretation of the *ZT* values. In order to measure all the properties along the *same* direction, we cut several bars of our samples and re-stuck them together after rotating the bars by 90 degrees using JB Weld® (a thermally conducting and electrically insulating glue). A detailed study of the measurements in different configurations using this glue can be found in our previous work[34]. The Hall measurements were performed on a Quantum Design® physical properties measurement system (PPMS) under a magnetic field sweep of ± 5 kOe. All measurements were performed on at least two independent sets of samples to confirm our transport data.

1. Tritt, T. M. Thermoelectric phenomena, materials, and applications. *Annual Review of Materials Research* **41**, 433 (2011).
2. Bhandari, C. M. & Rowe, D. M. in *CRC Handbook of Thermoelectrics*, Rowe, E. D. M. Ed. (CRC Press Inc, Boca Raton, FL, USA, 1995), pp. 43–53.
3. Ioffe, A. F. *Semiconductor thermoelements and thermoelectric cooling.* (Infosearch London, 1957).
4. Biswas, K. *et al.* High-performance bulk thermoelectrics with all-scale hierarchical architectures. *Nature* **489**, 414 (2012).
5. Puneet, P. *et al.* Enhancement of Thermoelectric Performance of Ball-Milled Bismuth Due to Spark-Plasma-Sintering-Induced Interface Modifications. *Advanced Materials* **25**, 1033 (2013).
6. Snyder, G. J. & Ursell, T. S. Thermoelectric efficiency and compatibility. *Physical review letters* **91**, 148301 (2003).
7. Snyder, G. J. Application of the compatibility factor to the design of segmented and cascaded thermoelectric generators. *Applied physics letters* **84**, 2436 (2004).
8. Snyder, G. J. in *Thermoelectrics handbook: macro to nano*, Rowe, E. D. M. Ed. (CRC press Inc., Boca Raton, FL, USA, 2006).
9. Goldsmid, H. J. & Douglas, R. W. The use of semiconductors in thermoelectric refrigeration. *British Journal of Applied Physics* **5**, 386 (1954).
10. Zhang, H. *et al.* Topological insulators in Bi2Se3, Bi2Te3 and Sb2Te3 with a single Dirac cone on the surface. *Nature Physics* **5**, 438 (2009).
11. Chen, Y. *et al.* Experimental realization of a three-dimensional topological insulator, Bi2Te3. *Science* **325**, 178 (2009).
12. Goldsmid, H. J. *Thermoelectric refrigeration.* (Plenum Press New York, 1964), vol. **1**.
13. Poudel, B. *et al.* High-thermoelectric performance of nanostructured bismuth antimony telluride bulk alloys. *Science* **320**, 634 (2008).
14. Tang, X. *et al.* Preparation and thermoelectric transport properties of high-performance p-type Bi2Te3 with layered nanostructure. *Applied Physics Letters* **90**, 012102 (2007).
15. Xie, W. *et al.* Identifying the specific nanostructures responsible for the high thermoelectric performance of (Bi, Sb) 2Te3 nanocomposites. *Nano letters* **10**, 3283 (2010).
16. Shen, J.-J. *et al.* Recrystallization induced in situ nanostructures in bulk bismuth antimony tellurides: a simple top down route and improved thermoelectric properties. *Energy & Environmental Science* **3**, 1519 (2010).
17. Shen, J. *et al.* Improved Thermoelectric Performance of p-Type Bismuth Antimony Telluride Bulk Alloys Prepared by Hot Forging. *Journal of electronic materials* **40**, 1095 (2011).
18. Zhang, B., He, J., Ji, X., Tritt, T. M. & Kumbhar, A. Controlled two-dimensional coated nanostructures for bulk thermoelectric composites. *Applied physics letters* **89**, 163114 (2006).
19. Ji, X., He, J., Su, Z., Gothard, N. & Tritt, T. M. Improved thermoelectric performance in polycrystalline p-type BiTe via an alkali metal salt hydrothermal nanocoating treatment approach. *Journal of Applied Physics* **104**, 034907 (2008).
20. Li, J.-F., Liu, W.-S., Zhao, L.-D. & Zhou, M. High-performance nanostructured thermoelectric materials. *NPG Asia Materials* **2**, 152 (2010).
21. Soni, A. *et al.* Interface driven energy filtering of thermoelectric power in spark plasma sintered Bi2Te2. 7Se0. 3 nanoplatelet composites. *Nano letters* **12**, 4305 (2012).
22. Wang, S., Xie, W., Li, H. & Tang, X. Enhanced performances of melt spun Bi2(Te,Se)3 for n-type thermoelectric legs. *Intermetallics* **19**, 1024 (2011).
23. Zhang, Z., Sharma, P. A., Lavernia, E. J. & Yang, N. Thermoelectric and transport properties of nanostructured Bi2Te3 by spark plasma sintering. *Journal of Materials Research* **26**, 475 (2011).
24. Yan, X. *et al.* Experimental studies on anisotropic thermoelectric properties and structures of n-type Bi2Te2.7Se0.3. *Nano letters* **10**, 3373 (2010).
25. Teweldebrhan, D., Goyal, V. & Balandin, A. A. Exfoliation and characterization of bismuth telluride atomic quintuples and quasi-two-dimensional crystals. *Nano letters* **10**, 1209 (2010).
26. Kuo, C.-H. *et al.* Thermoelectric transport properties of bismuth telluride bulk materials fabricated by ball milling and spark plasma sintering. *Journal of Alloys and Compounds* **496**, 687 (4/ 30/, 2010).
27. Coleman, J. N. Liquid Exfoliation of Defect-Free Graphene. *Accounts of Chemical Research* **46**, 14 (Jan 15, 2013).
28. Eda, G. *et al.* Photoluminescence from Chemically Exfoliated MoS2. *Nano letters* **11**, 5111 (Dec, 2011).
29. Minnich, A., Dresselhaus, M., Ren, Z. & Chen, G. Bulk nanostructured thermoelectric materials: current research and future prospects. *Energy & Environmental Science* **2**, 466 (2009).
30. Vineis, C. J., Shakouri, A., Majumdar, A. & Kanatzidis, M. G. Nanostructured Thermoelectrics: Big Efficiency Gains from Small Features. *Advanced Materials* **22**, 3970 (2010).
31. Goldsmid, H. & Sharp, J. Estimation of the thermal band gap of a semiconductor from Seebeck measurements. *Journal of electronic materials* **28**, 869 (1999).
32. Navratil, J., Stary, Z. & Plechacek, T. Thermoelectric properties of p-type antimony bismuth telluride alloys prepared by cold pressing. *Materials Research Bulletin* **31**, 1559 (12// 1996).
33. Matthiessen, A. On the electric conducting power of the metals. *Philosophical transactions of the royal society of London*, **148**, 383 (1858).
34. Xie, W. *et al.* Investigation of the sintering pressure and thermal conductivity anisotropy of melt-spun spark-plasma-sintered (Bi, Sb)2Te3 thermoelectric materials. *Journal of Materials Research* **26**, 1791 (2011).
35. Walker, P. The thermal conductivity and thermoelectric power of bismuth telluride at low temperatures. *Proceedings of the Physical Society* **76**, 113 (1960).
36. Leibfried, G. & Schloemann, G. Heat Conduction in Electrically Insulating Crystals. *Nach. Akad. Wiss. Gottingen. Math. Phys. Klasse.* **2a**, 71 (1954).
37. Berman, R. *Thermal Conduction in Solids.* (Clarendon Press, Oxford, 1976).
38. Russo, V. *et al.* Raman spectroscopy of Bi-Te thin films. *Journal of Raman Spectroscopy* **39**, 205 (2008).
39. Zheng, Z. *et al.* Optimization in fabricating bismuth telluride thin films by ion beam sputtering deposition. *Thin Solid Films* **520**, 5245 (2012).
40. Pope, A., Littleton, R. & Tritt, T. M. Apparatus for the rapid measurement of electrical transport properties for both "needle-like" and bulk materials. *Review of Scientific Instruments* **72**, 3129 (2001).
41. Pope, A., Zawilski, B. & Tritt, T. M. Description of removable sample mount apparatus for rapid thermal conductivity measurements. *Cryogenics* **41**, 725 (2001).
42. Mehta, R. J. *et al.* A new class of doped nanobulk high-figure-of-merit thermoelectrics by scalable bottom-up assembly. *Nature materials* **11**, 233 (2012).

Acknowledgments

Author contributions

P.P., R.P., and A.M.R. conceived and initiated the study. M.K. prepared all the exfoliated samples. P.P. and R.P. performed physical characterization of the samples. P.P. prepared the sintered samples and measured all the thermoelectric data. S.Z. measured low-temperature thermal conductivity. T.M.T. provided access to the low and high temperature electrical and thermal transport characterization facilities and the spark plasma sintering capabilities. P.P., R.P., M.S.D., J.H., and A.M.R. analysed the data. P.P. and R.P. wrote the manuscript. J.H., A.M.R., and M.S.D. edited the manuscript.

Additional information